Design and Fabrication of a MEMS-Based Break Junction Device for Mechanical Strain-Correlated Optical Characterization of a Single-Molecule

Hyunhak Jeong, Lucas K. Domulevicz, and Joshua Hihath, Senior Member, IEEE

Abstract— Here, we propose a robust lab-on-a-chip system for (electrical, multi-dimensional optical, and mechanical) characterization of a single-molecule utilizing a Si micromachined micro-electromechanical-system (MEMS) chip. Our MEMSbased break junction (MEMS-BJ) utilizes conventional MEMS chip fabrication techniques to create an electrostatic comb actuator capable of trapping a single-molecule between two nanoscale metal electrodes with sub-nanometer displacement resolution. In order to achieve this functionality, components of the chip (e.g flexural spring, comb drive fingers) are delicately designed based on an analytical model and basic performance parameters are verified using a finite element analysis simulation and capacitive sensor measurements. Using this system, we are able to perform combined single-molecule Raman spectroscopy and molecular conductance measurements in real-time. Finally, we present a representative case study of the multi-dimensional characterization of a single-molecule junction by analyzing correlated electrical, optical, and mechanical information while mechanically modulating the strain on the junction which allows for direct observation of the interplay between molecular structure and electron transport. We believe that our MEMS-BJ system will enable a deeper multi-dimensional study at a singlemolecule level promoting the development of new methods for chemical and biological sensor applications.

Index Terms— Finite element analysis, Molecular electronics, Microelectromechanical systems, Microfabrication, Raman scattering

I. INTRODUCTION

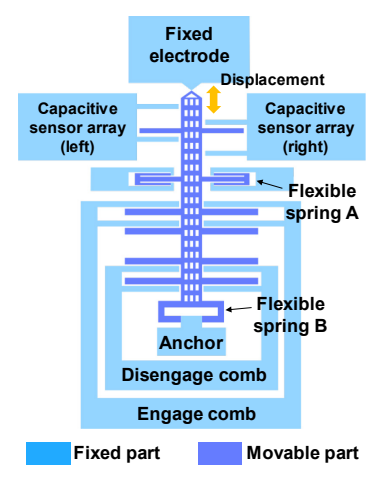
DISCOVERIES in the field of nanoscience are now leading the researcher to seek fundamental phenomena at the smallest possible condensed-matter scales that of the molecule or atom. To pursue this aim, ultra-small, high resolution platforms for manipulation and characterizations of nanomaterials have been utilized. For example, single-molecule characterization techniques such as scanning tunneling microscopy and advanced noncontact atomic force microscopy are proposed as a means for measuring the electrical

conductance of genetic materials and the direct imaging of chemical reactions, respectively [1, 2], and have gained great interest among researchers in this field. However, due to the size scale of the analyte and the associated complexity, it is inherently difficult to investigate its response to multiple stimuli (e.g. optical, electrical, and mechanical) simultaneously which are highly correlated with dynamic properties of molecules such as surface binding configurations and electronphonon interactions. Recently, further improvements have been pursued to realize such systems in the form of a lab-on-a-chip which will also present a unique opportunities for future electronics applications [3]. In this regard, microelectromechanical-system (MEMS) based actuators can be used for this purpose since they provide various advantages including high control resolution, architectural flexibility, and compatibility with conventional micromachining techniques which have already been used for biomedical applications such as microneedles [4, 5], lab-on-a-chip devices for fast analyte detection [6], and a lateral tunneling unit which can be utilized for nanomaterials characterizations [7].

In this work, we present the development of a robust lab-on-a-chip system for multi-dimensional (electrical, optical, and mechanical) characterization of a single-molecule utilizing a Si micromachined MEMS chip on a silicon-on-insulator (SOI) wafer. The methodology to realize this MEMS-based break junction (MEMS-BJ) utilizes conventional MEMS chip fabrication techniques, to create an electrostatic comb actuator that can trap a single-molecule between two nanoscale metal electrodes with sub-nanometer displacement resolution. In order to achieve this capability, components of the chip (e.g flexural spring, comb drive fingers) are delicately designed based on an analytic model and basic performance parameters are verified using a finite element analysis (FEA) simulation

Manuscript received XX; revised XX; accepted XX. Date of publication XX; date of current version XX. Authors acknowledge funding from the U.S. Office of Naval Research (N000141612658), the NSF/SRC SemiSynBio program (1807555/2836), and the NSF-CBET division (1605338).

The authors are with the Department of Electrical and Computer Engineering, University of California, Davis, 1 Shields Avenue, Davis, CA 95616 USA (e-mail: jhihath@ucdavis.edu).



Scheme 1. Schematic illustration of MEMS-BJ system.

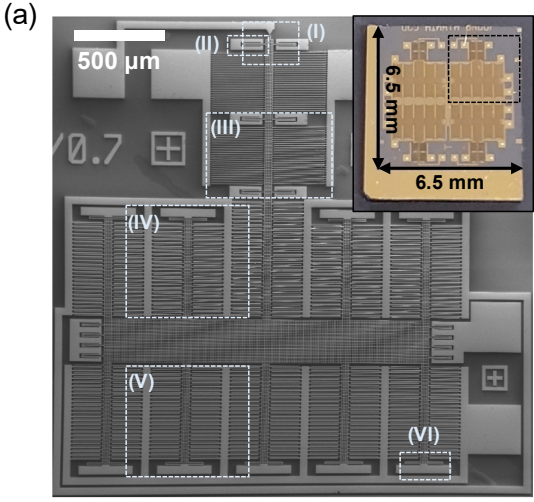
and capacitive sensor measurements. Using the system, we conduct one of the distinctive applications for our system: combined single-molecule Raman spectroscopy and molecular conductance measurements in real-time. Finally, we demonstrate an example study of the multi-dimensional characterization of a single-molecule junction by correlating electrical, optical and mechanical information while mechanically modulating the strain on the junction which allows for the direct observation of the interplay between molecular structure and electron transport.

II. DESIGN

A. Design and Operation Principle

A schematic illustration of the MEMS-BJ system is depicted in Scheme 1. The system is composed of five fundamental components: a movable electrode, a fixed electrode, a capacitive sensor array, a flexural spring, and an electrostatic comb drive array. To realize sub-nanometer displacement resolution and controllability with sufficient forces to rupture a suspended gold bridge (details will be explained later), an electrostatic comb actuation scheme was implemented. In particular, we utilize a transverse comb drive in which the comb fingers move perpendicular to the longitudinal axis of the set of fixed fingers in order to produce a larger force but smaller displacement [8].

Fig. 1 shows optical and scanning electron microscopy (SEM) images of each main components of a MEMS-BJ chip. The chips are fabricated using standard solid-state Si micromachining techniques on an SOI wafer. Each chip is composed of four identical devices. For the suspended gold bridge, a well-known bowtie structure is utilized to precisely define the location of the fracture and gap formation (Fig. 1(c)) [9]. Additionally, we designed two opposing comb drive configurations (denoted as engage combs and disengage combs in Fig. 1(b), respectively) on the chip, which allows us to produce movement in either direction. Lastly, the upper portion of the system incorporates a parallel-plate capacitive sensor array to measure the displacement.



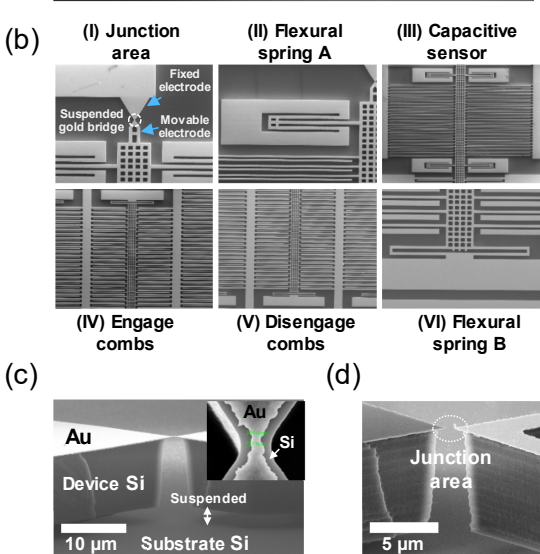


Fig. 1. Optical and SEM images of each main component in a MEMS-BJ chip. (a) SEM image of a MEMS-BJ device. Inset shows the optical image of a chip. (b) Magnified SEM images of each component of the chip labeled in (a). (c) Tilted view of the suspended gold bridge after suspension. Inset shows the zoomed-in image of the bowtie structure in the junction area before removing underneath device Si layer. (d) Tilted view of the suspended gold bridge after several tapping measurements. As shown in the figure, some of the central part of the suspended gold bridge is missing due to the mechanical stress involved in the tapping measurements.

B. Detailed Design Parameters

In this work, we designed our MEMS-BJ chips to meet the following constraints: (i) a target tensile strength of 220 MPa to be able to fracture a suspended gold bridge and generate a molecular gap, (ii) several hundred nanometers travel range within a pull-in voltage of 100 V, and (iii) to provide an actuation resolution of < 50 nm/V for nanometer-scale controllability [10]. In this regard, we first considered the induced electrostatic force. Fig. 2 shows a schematic of a unit of the disengage comb drive electrode array. The induced electrostatic force F at an actuation voltage V is given by

$$F = \frac{1}{2} \frac{\varepsilon_0 N a}{(d-x)^2} V^2 = \frac{1}{2} \frac{\varepsilon_0 N l t}{(d-x)^2} V^2$$
 (1)

where x is the displacement, d is the gap distance, N is the number of comb fingers, l is the overlapping length, t is the

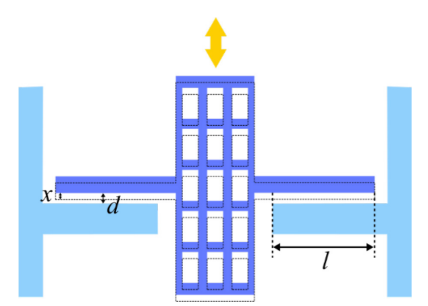


Fig. 2. Schematic of a unit of disengage comb drive electrode array.

TABLE I

SUMMARY OF THE DESIGN PARAMETERS AND DIMENSIONS		
Design component	Design parameter	Value
(II) Flexural spring A	Beam width: w (μm)	5
	Beam length: l_{a1} (µm)	135
	Beam length: l_{a2} (µm)	105
	Number of spring: N_{A}	14
(VI) Flexural spring B	Beam width: w (μm)	5
	Beam height: h (µm)	15
	Beam length: l_b (µm)	120
	Number of spring: $N_{\rm p}$	9
(IV), (V) Engage/Disen gage combs	Overlap length of parallel comb fingers: $l(\mu m)$	150
	Gap between electrode: <i>d</i> (μm)	2.5
	Number of comb fingers: N	150
(III) Capacitive sensor	Narrow gap distance: d_1 (µm)	2.5
	Wide gap distance: d_2 (µm)	5.5
	Overlap length of parallel sense	300
	fingers: L (μm)	
	Number of sense fingers: N _c	51
	Thickness of device Si layer: t (μm)	10

thickness of the device Si layer, and a is the overlapping area between comb finger electrodes. Typically, the constriction of the narrowest gold bridge was 300-500 nm wide and 200 nm thick which requires a maximum tensile force of 22 µN to rupture a suspended gold bridge assuming the ultimate tensile strength of gold is 220 MPa [11].

In order to meet the second condition correlated with the induced electrostatic force, we design two different types of flexural springs [8]. Fig. 3 shows SEM images of each flexural spring and their equivalent lumped model. Each spring is designed or arranged symmetrically in a chip along the y-axis line crossing the center of the bowtie structure in order to nullify x-axis displacement. The in-plane (along y-axis) and out-ofplane (along z-axis) spring constants of each flexure is given by,

Flexural spring A

$$k_{Ay} = \frac{2k_{a2y}k_{a1y}}{2k_{a2y}+k_{a1y}}, \quad k_{aiy} = \frac{Etw^3}{l_{ai}^3} \quad (i = 1, 2)$$

$$= Etw^3 \left(\frac{2}{2l_{a1}^3 + l_{a2}^3}\right) \tag{2}$$

$$k_{Az} = \frac{2k_{a2z}k_{a1z}}{2k_{a2z}+k_{a1z}}, \quad k_{aiz} = \frac{Ewt^3}{l_{ai}^3} \text{ (i = 1, 2)}$$
$$= Ewt^3 \left(\frac{2}{2l_{a1}^3 + l_{a2}^3}\right) \tag{3}$$

Flexural spring B:

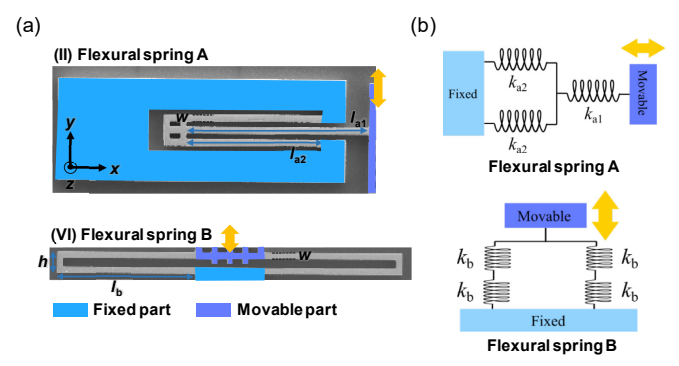


Fig. 3. (a) SEM images of two flexural springs and (b) their equivalent lumped

$$k_{\rm By} = \left(\frac{1}{k_{\rm by}} + \frac{1}{k_{\rm by}}\right)^{-1} + \left(\frac{1}{k_{\rm by}} + \frac{1}{k_{\rm by}}\right)^{-1} = k_{\rm by}$$
 (4)

$$k_{\rm Bz} = \left(\frac{1}{k_{\rm bz}} + \frac{1}{k_{\rm bz}}\right)^{-1} + \left(\frac{1}{k_{\rm bz}} + \frac{1}{k_{\rm bz}}\right)^{-1} = k_{\rm bz}$$
 (5)
$$k_{\rm by} = \frac{Etw^3}{l_{\rm b}^3}, \ k_{\rm bz} = \frac{Ewt^3}{l_{\rm b}^3} \ (l_{\rm b} \gg h)$$
 (6)

$$k_{\rm by} = \frac{Etw^3}{l_{\rm b}^3}, \ k_{\rm bz} = \frac{Ewt^3}{l_{\rm b}^3} \ (l_{\rm b} \gg h)$$
 (6)

where E is the Young's modulus of the highly doped Si (130 GPa). Then, effective in-plane and out-plane spring constants of the system are given by,

$$k_{y} = N_{A}k_{Ay} + N_{B}k_{By} = Etw^{3} \left(\frac{2N_{A}}{2l_{a1}^{3} + l_{a2}^{3}} + \frac{N_{B}}{l_{b}^{3}}\right)$$
 (7)

$$k_{\rm z} = N_{\rm A} k_{\rm Az} + N_{\rm B} k_{\rm Bz} = Ewt^3 \left(\frac{2N_{\rm A}}{2l_{\rm a1}^3 + l_{\rm a2}^3} + \frac{N_{\rm B}}{l_{\rm b}^3} \right)$$
 (8)

where N_A and N_B are the number of the flexural spring A and B in a device, respectively. Considering the analytic model and design constraints above, the dimensions of the device components are determined. A summary of the design parameters and dimensions are provided in Table I. Here, we designed the out-of-plane spring constant to be higher than the in-plane spring constant in order to minimize potential z-axis drift in the junction area due to fringing field effects. Using these dimensions, we calculated the electrostatic force to be ~63.75 µN at a 20 V actuation voltage without any displacement (x) as assumed in (1), indicating that our MEMS-BJ device can generate a sufficient electrostatic force to rupture a suspended gold bridge. Another important parameter in the parallel plate electrostatic comb actuation system is a pull-in voltage $V_{\rm PI}$ given by,

$$V_{\rm PI} = \sqrt{\frac{8}{27} \frac{k_{\rm y} d^3}{\varepsilon_0 a}} = \sqrt{\frac{8}{27} \frac{k_{\rm y} d^3}{\varepsilon_0 lt}}$$
 (9)

This gives the pull-in voltage of ~60.88 V for the established parameters and satisfies constraint (ii). Finally, a simple force equilibrium condition gives the equilibrium displacement x at a specific actuation voltage by,

$$F = k_{y}x = \frac{1}{2} \frac{\varepsilon_{0}Nlt}{(d-x)^{2}} V^{2}$$
 (10)

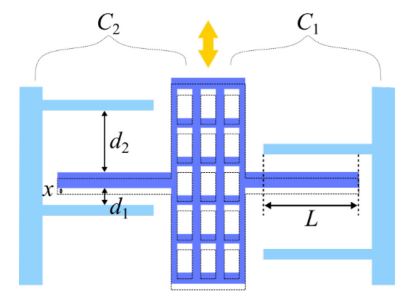


Fig. 4. Schematic design of the capacitive sensor comb configuration.

For example, at a 50 V actuation voltage, the equilibrium displacement is calculated as ~332.5 nm which satisfies constraints (ii) and (iii).

C. Capacitive Sensor Design

Fig. 4 shows a schematic of the capacitive sensor comb configuration. A differential capacitance sensing scheme is exploited to mitigate the parasitic capacitance effects [12]. Since this technique provides the high sensitivity and linearity to the displacement, many applications such as a microforce sensing [13], and nano-biomaterials characterizations [14, 15] have been utilized it. When the displacement, x, is much smaller than the gap distance d_1 and d_2 , while neglecting fringing field effects, the differential capacitance can be approximated from the following equation:

$$\Delta C = C_2 - C_1 = \varepsilon_0 N_c A \left(\frac{1}{d_1 - x} + \frac{1}{d_2 + x} - \frac{1}{d_1 + x} - \frac{1}{d_2 - x} \right)$$

$$\cong \varepsilon_0 N_c Lt \left(\frac{1}{d_1^2} - \frac{1}{d_2^2} \right) x \tag{11}$$

where N_c is the number of capacitive sensor comb fingers, L is the overlapping length, t is the thickness of the device Si layer, and A is the overlapping area between each capacitive sensor finger electrode. Then, the dimension of the capacitive sensor comb finger is determined by assuming the required displacement resolution of 0.2 nm and maximum capacitance resolution of ~ 50 aF at 100 Hz tapping measurement (the nominal capacitance resolution of the integrated circuit (IC) is $4.0 \text{ aF/}\sqrt{\text{Hz}}$). Table I gives the dimensions of the capacitive sensor comb fingers. In this case, the calculated capacitance change is $\sim 68.8 \text{ aF}$ corresponding to 0.2 nm displacement.

III. SIMULATION

The device performance is further analyzed using a FEA software package (COMSOL Multiphysics). First, fundamental characteristics related to the device operation, such as a tensile stress at the fracture point in the junction area, are analyzed (inset of Fig. 5(a)) to verify our design if the system can generate an enough strength over the ultimate tensile strength of gold in a reasonable range of the actuation voltage under the pull-in voltage. Here, we consider a suspended gold bridge with a width of 1 µm at its narrowest point and a thickness of 200 nm. The uniaxial tensile stress of the gold layer is set to 220 MPa and the Willam-Warnke yield criterion model is assumed to analyze the deformation and failure of the bridge [16]. This model is for describing concrete failure of cohesive-fractional

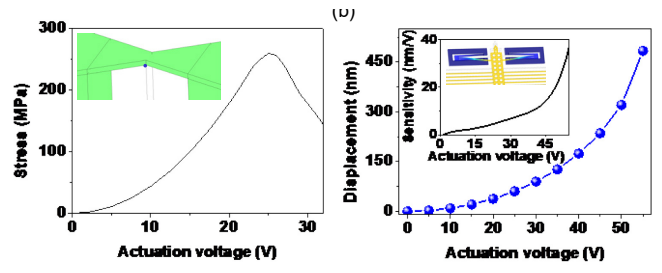


Fig. 5. FEA simulation results. (a) Calculated tensile stress at the fracture point. (b) The longitudinal displacement of the fracture point after a rupture versus the actuation voltage with corresponding sensitivity from the simulation result (inset). The schematic in the inset shows an exaggerated illustration of the displacement at 50 V actuation bias.

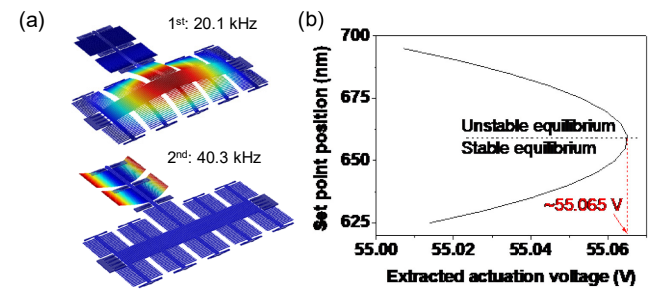


Fig. 6. FEA simulation results. (a) Calculated 1st and 2nd natural frequencies of a MEMS-BJ device. (b) Equilibrium relationship between set point position and actuation voltage calculated by solving an inverse problem.

materials ensuring constitutive law for elastic but perfectly brittle behavior in tension. Since the evaporated gold thin layer is a cohesive-fractional material and brittle since it is composed of single-crystal grains aggregated together, this model might be suitable model for describing failure of our suspended gold bridge. From the simulation results as shown in Fig. 5(a), it is found that the fracture point starts necking from the actuation voltage at ~25 V as can be seen from the decreasing stress from this point. Note that, however, the experimental force characterization is essential to verify the simulation and our design including dimension control as a future work. Fig. 5(b) depicts an anticipated displacement of the fracture point versus the actuation voltage with its associated sensitivity after a rupture of the junction. From the simulation results, we found that the simulated displacement shows a similar value compared to the analytic model satisfying constraints (ii) and (iii) in Design section above. Because the electrostatic force is proportional to the square of the actuation voltage, as the displacement increases, the sensitivity also increases with increasing actuation voltage.

Another important aspect in the MEMS-BJ system is the electromechanical stability of the device. Modal analysis is performed to investigate the natural frequencies of the device as shown in Fig. 6(a). From the simulations, it is found that the first mode is an out-of-plane sagging of the movable mesh structure with a modal frequency of 20.1 kHz due to its own weight which leads to twisting of the whole structure. The next mode is a longitudinal mode with associated modal frequency of 40.3 kHz. Stiff suspensions (i.e. stiff flexural springs) and small device masses in the MEMS chip can yield relatively high natural frequencies in our device which make the chip

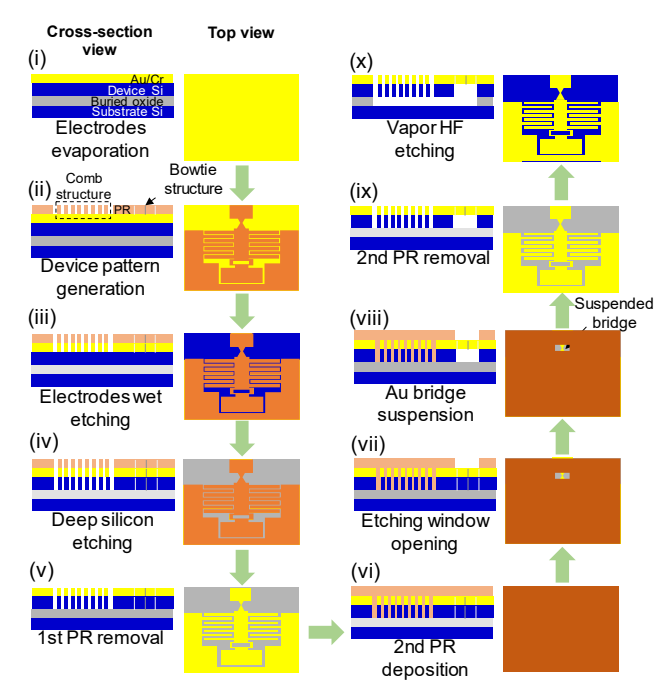


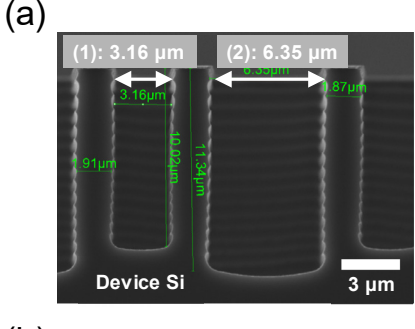
Fig. 7. Chip fabrication procedure.

insensitive to the environmental vibrational sources [17].

Finally, the pull-in voltage $V_{\rm PI}$ is simulated by solving an inverse problem. In this case, the solver computes the required actuation voltage in order to generate certain displacements of the fracture point. Solving the problem in this way prohibits the convergence failure of the solver in the case of no solutions (i.e. applying the actuation voltage exceeding the pull-in voltage) [18]. Fig. 6(b) shows the simulation results. The set point position (*y*-axis) represents an arbitrary *y*-coordinate to solve the inverse problem. From the plot, it is found that the simulated pull-in voltage is ~ 55.07 V which is close to the value determined from the analytic model, satisfying constraint (ii) in the section II. The discrepancy observed may be due to the approximation of the spring constants in the calculation and the neglecting of fringing field effects.

IV. FABRICATION

Fig. 7 illustrates an overview of the chip fabrication procedure. (i) The fabrication starts by depositing a layer of gold/chromium (200/5 nm) on a SOI wafer for the electrode (10 μm thick heavily doped p-type device Si layer, and 2 μm thick buried oxide (BOX) layer), using an e-beam evaporation technique. In order to exploit the device Si layer as comb fingers for actuation, heavily doped p-type poly silicon was used in the device layer. (ii) A conventional photolithography technique was utilized to generate the device pattern on the metal electrode layer using the first photoresist (PR) layer (SPR 955-CM 0.7, from Rohm and Haas Electronic Materials LLC). To do this, first, the PR is spin-coated on the metal electrode layer at 3400 rpm for 50 secs followed by soft-baking it on a hot plate at 110 °C for 60 secs. Next, the chip is exposed to i-line (365 nm) UV light to draw the device pattern for 0.28 secs at 550 mW/cm² intensity (GCA 8500 i-line stepper). After that, the



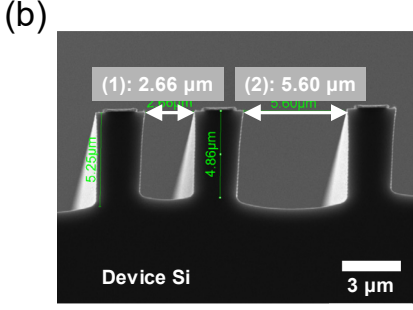
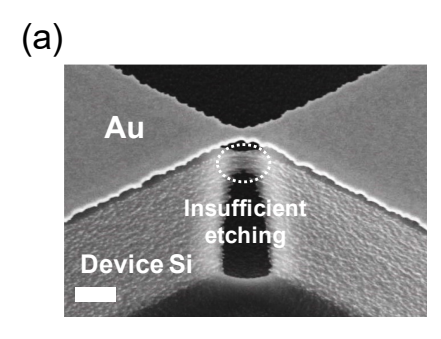


Fig. 8. Cross-sectional SEM images of the capacitive comb sensor array. (1) is the narrow gap d_1 which is supposed to be 2.5 μ m wide from the design (Table 1). (2) is the wide gap d_2 which is supposed to be 5.5 μ m wide from the design (Table 1). In case of no reflow of the first PR layer the comb structure is over-etched during the DSE process (a) while that is correctly etched with the reflow (b).

chip undergoes a post exposure baking at 110 °C for 90 secs. The device pattern is developed by dipping and agitating the chip in a developer (CD-26, from Rohm and Haas Electronic Materials LLC) for 60 secs, and then immediately rinsing it with deionized (DI) water. After that, the pattern is hard-baked on a hot plate at 110 °C for 3 min. The minimum width of the bowtie structure is 1 µm. (iii) To pattern the metal electrode, we etch the revealed metal electrode surface by immersing and agitating the chip in wet etchants for each metal layer. First, 10 vol.% of Gold Etchant TFA (from Transene company Inc.) in DI water is used for etching the revealed gold layer. The etching time is varied from 75 to 120 secs until the revealed gold surface is completely etched by observing the color change. Here, note that a delicate optimization of this etching time is crucial to determine the chip operation modes because the wet etching process inevitably induces an undercut in the bowtie structure. If the undercut etching is excessive, the bowtie structure may be initially disconnected which makes the chip only operational in the engage mode. Nevertheless, this approach allows us to achieve a narrower width in the bowtie structure which will facilitate an easy fracture of the suspended gold bridge. Subsequently, the chromium layer is wet-etched in a Chromium Etchant 1020 (from Transene company Inc.) for 5 secs. (iv) Then, a deep silicon etching (DSE) process is performed to vertically etch down the device Si layer to form structural parts of the MEMS-BJ chip using the Bosch process (PlasmaTherm Versaline Deep Silicon Etcher) [19]. Each cycle exhibits ~500 nm deep vertical etching of the Si layer with less scallops and a total of 24 cycles are performed to completely etch the Si layer down to the BOX layer. Here, it is important to note that we



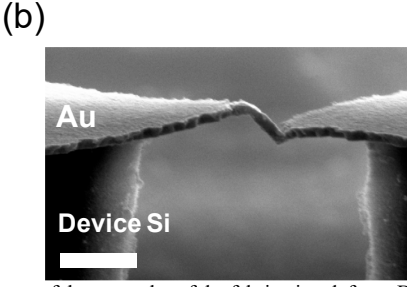


Fig. 9. SEM images of the examples of the fabrication defects. Both scale bars represent 1 μ m. (a) Insufficient etching in the junction area. The device Si layer underneath the bowtie structure is not fully etched. (b) Misalignment of a gold bowtie structure due to the residual stress while releasing the device Si layer from the substrate Si layer.

anneal the sample at 110 °C for 3 min before performing the DSE process. This procedure allows the PR layer reflow to cover the gap between the sacrificial PR layer and device Si layer along the device pattern edge which is generated due to undercut etching of the metal electrode layer [20]. Otherwise, the structural parts will be over-etched deforming the performance of the chip (Fig. 8). (v) Finally, the remaining first PR layer is removed by dissolving the PR in a positive resist stripper (PRS-3000, from J. T. Baker) at 80 °C for 10 min. After the removal, the chip is thoroughly rinsed using DI water. (vi) The second PR layer for a selective isotropic etching of the device Si layer is deposited. In order to achieve uniformly filled PR layer in the high aspect ratio MEMS-BJ body structures, we use two different types of PR with a different viscosity. First, we spin-coat the chip with a less viscous PR (SPR 955-CM 0.7) three times at 3400 rpm for 50 secs each. Each coated PR layer is soft-baked on a hot plate at 110 °C for 60 secs. Since this PR has a less viscosity, the PR solution can easily fill in the 10 μm thick comb structure (maximum 1:4 aspect ratio) without bubbles. This makes the surface of the device Si layer more hydrophobic which eventually allows the second PR with a higher viscosity uniformly wet to the layer. Next, the second PR with a higher viscosity (SPR 220-7.0, from Rohm and Haas Electronic Materials LLC) is spin-coated on the chip at 2500 rpm for 60 secs followed by soft-baking at 105 °C for 360 secs. By adopting this two-stage deposition method, we can uniformly cover the entire chip surface area. (vii) Subsequently, a conventional photolithography technique is used with a contact aligner to expose the chip to UV light for 600 mJ/cm². To develop the pattern, we submerge and agitate the chip in a developer (CD-26) for 180 secs, and immediately rinse the chip using DI water. This process opens a window exclusively near

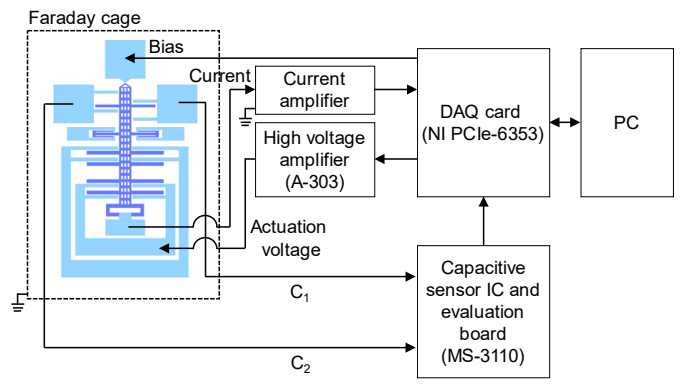


Fig. 10. Circuit schematic of the measurement system.

the gold bridge area to selectively etch the device Si layer underneath the gold bridge. (viii) The gold bridge is suspended by isotropic etching of the Si layer underneath the gold bridge using a reactive ion etching (RIE) technique (330 mTorr, 8 sccm of CF₄ gas, 1 sccm of O₂ gas, 50 W, 240 secs). Due to the isotropic etching property of the RIE technique, we can suspend the narrow gold bridge area to precisely define where the fracture occurs (Fig. 1(c)). Fig. 9(a) shows an SEM image of the case of insufficient etching. (ix) The remaining second PR layer is removed by dissolving the PR in a positive resist stripper (PRS-3000) at 80 °C for 20 min. After the removal, the chip is thoroughly rinsed using DI water. (x) Finally, the entire structure, except for the anchoring portions, is released from the substrate by vapor phase hydrofluoric acid (HF) etching of the BOX layer (Idonus HF vapor etch). To do this, the chip is mounted on a warm flat stage at 40 °C and then the mounted chip is flipped face down in a liquid HF solution (49 %) surface from ~ 1 cm above. The process is continued for ~ 40 min under ambient conditions. Here, note that even though the BOX layer will be etched slowly without sticking to the substrate Si layer using this technique, there can be potential distortions in the device including the misalignment of the gold tips as shown in Fig. 9(b) due to the residual stress.

V. EXPERIMENT

A. Measurement System

The circuit schematic of the measurement system for the electrical characterization is shown in Fig. 10. A PC-controlled commercial data acquisition (DAQ, NI PCIe-6353) card with 16-bit ADC/DAC (±10 V range) was used to acquire and send voltage signals to the system. For the electrical measurement, the fabricated chip was mounted onto a 24-pin IC chip carrier socket in a lab-constructed circuit board, shielded by a faraday cage. A commercial low-noise high voltage amplifier (A-303, A.A. Lab systems) with a constant gain of ~20 was used to apply a high actuation voltage to the comb drive electrodes depending on the actuation mode (i.e. engage mode versus disengage mode). In order to measure the electrical conductance of a molecular junction, a bias voltage was applied to the fixed electrode while the movable electrode was maintain at virtual ground. Then, the current through the junction was converted into a voltage signal by a simple OP-amp based transimpedance amplifier with gains of either ~10 nA/V or 100

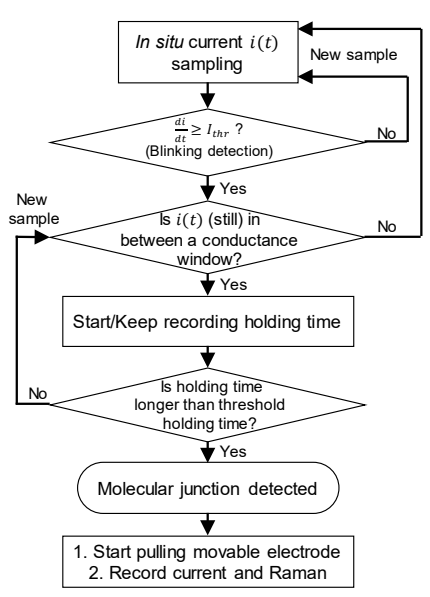


Fig. 11. Decision chart for detection and pulling of a molecular junction implanted in the LabVIEW program.

nA/V. For the capacitive sensor measurement, differential capacitance was measured by the opposite excitation scheme of each capacitive sensor array with a square-wave signal. Since the excitation signal frequency (100 kHz) is much higher than the actuation and resonance frequency in Fig. 6(a) and the actuation voltage is applied with the consideration of the excitation signal (i.e. V_s), we neglect the displacement resulting from the capacitive sensor measurement. Finally, all the electrical measurements, signal controls, and data analysis were performed using custom LabVIEW programs at the ambient air and room temperature.

B. Tapping Measurement and Deposition of Molecules

We statistically measure the electrical conductance traces of nanoscale junctions by applying an alternating actuation voltage to the comb electrodes to repeatedly bring the two electrodes into and out of contact (so-called "tapping-cycle"). The actuation voltage is altered depending on whether the tunneling current is saturated (gold-gold contact) or disappeared (junction breakdown). Also the tip is brought out from the contact immediately after the tunneling current is saturated to reduce a deformation of the tips due to a severe mechanical stress involved in the tapping cycles. But still, it is found that the mechanical stress is strong that it results in some deformation such as destroying of the central part of the suspended gold bridge as shown in Fig. 1(d). Therefore, a statistical approach to extract the characteristics of a singlemolecule junction is essential when we use our MEMS-BJ system. Each tapping trace is recorded when the movable electrode is brought out of contact (10 V/s ramp rate) assuring that the least conductance plateau before the junction breakdown (i.e. disappearing of the tunneling current) is a single-molecule conductance if we assume there is no serial binding of the molecules. Here, we use Biphenyl-4,4'-dithiol (BPDT) and Tetrahydrofuran as the target molecule and solvent, respectively. Prior to the measurement, we deposit the molecule on a MEMS-BJ chip by spraying a molecular solution (5 mM) onto the chip using a commercially available air-brush based atomizer (from Master Airbrush). The airbrush emit the molecular solution through a small hole along with compressed air (2-3 kPa) converting the liquid into a fine mist. Due to a small size of the fine mist, the solvent is easily vaporized and vented away while the molecules are deposited on the chip without inducing stiction. Usually we spray the molecular solution ~30 cm away from a MEMS-BJ chip with ~45° angle for 10 secs in a vented hood. Then during the tapping-cycle, the molecule can be stochastically trapped between the two electrodes, exhibiting a specified molecular conductance associated with the electronic structure of the molecule. Here, note that there should be a following investigation if the molecules are truly deposited successfully on the surface of the suspended gold bridge by employing a direct method to chemically detect the molecular species such as energydispersive X-ray spectroscopy.

C. Mechanism of Detection and Pulling of a Molecular Junction

The formation of a molecular junction is a highly stochastic process, in which a single-molecule is randomly trapped between metal electrodes while the molecule is wandering due to the surface diffusion and the life time of the molecular junction is usually short (several seconds). Therefore, an automated algorithm to detect and pull the molecular junction is necessary for determining the effects of mechanical pulling on the Raman spectrum. Considering the stochastic nature of the formation of a molecular junction, we can utilize an abrupt change of junction current to trigger an investigation of a molecular junction formation. Fig. 11 shows the decision chart for detection and pulling of a molecular junction. First, when an abrupt increase of the junction current is detected by observing that the first derivative of the current is higher than a threshold current derivative Ithr (blinking detection), the algorithm observes the junction current if this falls in a specified molecular conductance window. If so, the algorithm starts or continues to monitor the current to determine if the junction current sustains over a certain amount of time in the conductance window (i.e. conductance plateau). Finally, once the plateau is observed, the molecular junction is pulled by increasing or decreasing (in case of disengage/engage mode) the actuation voltage at a set pulling rate (in the unit of V/s) for a specified duration. During this process, Raman and

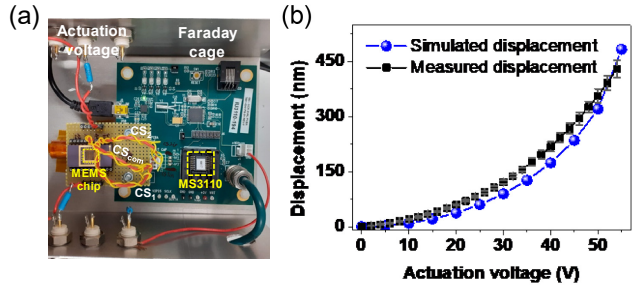


Fig. 12. (a) Optical image of capacitance sensing IC for capacitive sensor measurement in a Faraday cage. (b) Extracted relative displacement from the capacitive sensor measurement versus applied actuation voltage (black square box). The simulated displacement in Fig. 5(b) is replotted to compare each other (blue circle).

conductance data are simultaneously recorded in order to relate the effects of strain on conductance and molecular structure.

VI. RESULTS AND DISCUSSION

A. Capacitive Sensor Measurement

To verify the simulated displacement characteristics, our device is displaced by applying the actuation voltage to the comb fingers and the corresponding capacitance change is measured using the capacitance sensing IC (MS3110, Irvine Sensors, Costa Mesa, CA). Here, a differential capacitance sensing scheme is utilized and the connection between the chip and the IC are kept as short as possible to mitigate the parasitic capacitance effects while the parts are electrically shielded in a Faraday cage as shown in Fig. 12(a) [12]. The output voltage, $V_{\rm o}$, from the MS3110 are expressed in the following equation:

$$V_{\rm o} = G \times V_{\rm s} \times 1.14 \times \frac{c_2 - c_1}{c_{\rm F}} + V_{\rm REF}$$
 (12)

where G is the output gain, V_s in the square-wave excitation voltage amplitude, $C_{\rm F}$ is the feedback capacitance, and $V_{\rm REF}$ is the reference voltage. For the measurement, the values were set to G = 2, $V_s = 2.25$ V, $C_F = 5.13$ pF, $V_{REF} = 2.25$ V, respectively. Therefore, the capacitance change is given by,

$$\Delta C = C_2 - C_1 = V_0 - V_{RFF} \tag{13}$$

 $\Delta C = C_2 - C_1 = V_0 - V_{\text{REF}}$ (13) where C_1 and C_2 are in the unit of pF, and V_0 and V_{REF} are in the unit of V. Finally, substituting ΔC from (11) gives, $x = \frac{1}{2\varepsilon_0 N_{\rm c} A} \left(\frac{d_2^2 - d_1^2}{d_1^2 d_2^2} \right) \times (V_{\rm o} - V_{\rm REF})$ Ideally, the output voltage at no actuation voltage should be

$$x = \frac{1}{2\varepsilon_0 N_{\rm c} A} \left(\frac{d_2^2 - d_1^2}{d_1^2 d_2^2} \right) \times (V_0 - V_{\rm REF})$$
 (14)

equal to V_{REF} (=2.25 V) given a perfectly symmetric structure for the left and right capacitive sensor comb fingers (i.e. C_2 = C_1 at no actuation voltage) of our device. In reality, parasitic capacitances residing in between the sense and common lines (i.e. between CS₂ and CS_{com}; CS₁ and CS_{com} in Fig. 12(a)) and fabrication inconsistency-oriented capacitance mismatch disturbs the exact measurement of the differential capacitance in (13). Hence, relative displacement is a more accurate parameter for describing the response due to the applied

actuation voltage given in the following equation:

$$\Delta x = \frac{1}{2\varepsilon_0 N_c A} \left(\frac{d_2^2 - d_1^2}{d_1^2 d_2^2} \right) \times (V_0(V_a = 0) - V_0(V_a))$$
where V_a is the actuation voltage.

Fig. 12(b) shows the extracted relative displacement from the measurement versus the applied actuation voltage plot. During the test, the DC actuation voltage is applied to the disengage

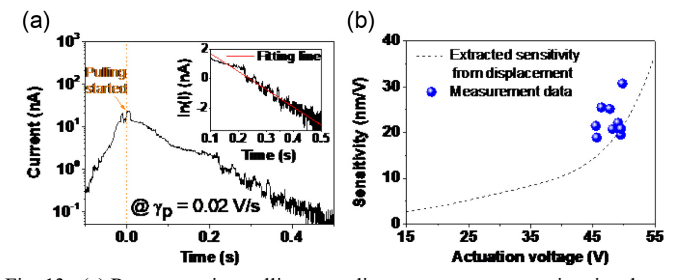


Fig. 13. (a) Representative pulling tunneling current trace over time in a bare gold-gold junction. Inset shows logarithmic value of the tunneling current over time with a fitting curve. (b) Extracted sensitivity of the device from nine different measurements of pulling tunneling current (blue circles). Calculated sensitivity curve in the inset of Fig. 5(b) is depicted once again for comparison (black dashed line).

combs (the suspended gold bridge is fractured prior to the measurement) from 0 to 54 V in incremental steps of 2 V. Then, each output voltage is recorded when they are steady and averaged over multiple times. From the plot, it is found that the measured displacement is proportional to the square of the applied actuation voltage and follows the similar trend to the simulated displacement in Fig. 5(b). Note that, however, there is a small discrepancy between the measurement and simulation results possibly caused by under-etching of the comb structures during DSE process which will produce a larger displacement than an ideal case.

B. Pulling Measurement of a Bare Gold-Gold Junction

To verify that the pulling scheme is working properly, we perform a model study of a bare gold-gold contact. In this measurement, decaying behavior of the tunneling current of a bare gold-gold contact depending on the increment of tunneling barrier width is investigated. At a constant bias voltage, the tunneling current through a nanoscale junction can be expressed by the following equation [21]:

$$I(d) = I_0 \exp(-\beta d) \tag{16}$$

where β is the tunneling decay coefficient of the tunneling barrier, d is the tunneling barrier width, and I_0 is the scaling factor. In the case of increasing tunneling barrier width (i.e. pulling), the equation can be expressed as:

$$I(d) = I_0 \exp(-\beta d)$$

= $I_0 \exp\{-\beta (d_0 + s\gamma_p t)\}$ (17)

where d_0 is the initial tunneling barrier width, s is the sensitivity (nm/V) of our MEMS-BJ device, γ_p is the pulling rate (V/s), and t is the pulling time (s). Therefore, the slope of the ln(I) versus t trace gives $-\beta s \gamma_p$ which can be used for the calibration and confirmation of the MEMS-BJ device performance.

Fig. 13(a) shows a representative current vs. pulling trace for a bare gold-gold junction. When a blinking event is detected (at t = 0 s) by the described algorithm above, the movable electrode is slowly pulled away from the fixed electrode with a constant pulling rate of 0.02 V/s. From the plot, it is found that the tunneling current shows an exponential decay as a function of time. The slope of this decay is fit in a semi-log plot as shown in the inset to extract the exponential factor (β) . Using (17) and the fitted slope values, we extract the sensitivity of the device from nine different measurements as shown in Fig. 13(b). Here, the tunneling decay coefficient of air is 2.9 Å⁻¹ and the actuation

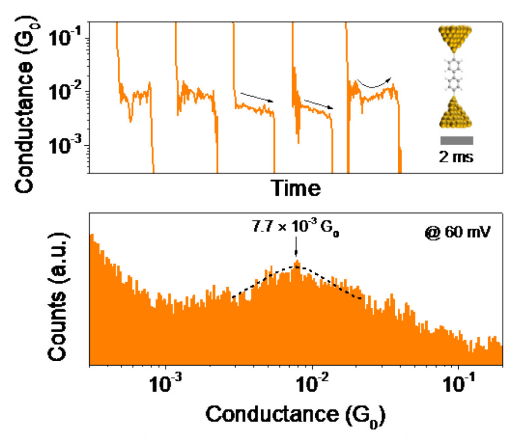


Fig. 14. Conductance histogram of BPDT. Top panel: Representative curves of selected tapping traces. Black arrows in some curves depict evolution of the tunneling current in the molecular junction upon elongation. Bottom panel: Constructed histogram from the selected traces.

voltage at each starting point of pulling is used as the actuation voltage [22]. From the plot, it is shown that the extracted sensitivity values from the measurements match well with the calculated sensitivity curve in Fig. 5(b), which supports the expected device performance from the simulation and capacitive sensor measurement. Nevertheless, there is a small discrepancy which possibly originates from a fabrication errors.

C. Tapping measurement

Equipped with the initial electromechanical characterization results for the MEMS-BJ chip, we test the basic suitability of our MEMS-BJ for molecular junction characterization by performing single-molecule conductance measurements. Fig. 14 shows representative tapping traces of gold-molecule-gold contacts and an accumulated electrical conductance histogram from a set of 1501 tapping traces at 60 mV bias. As shown in the upper panel of Fig. 14, some tapping traces show conductance plateaus at a specified conductance around ~7 × $10^{-3}G_0$, where G_0 (= $2e^2/h$, e is elementary charge and h is Planck constant) is the conductance quantum. From the histogram constructed by a set of such traces, we found a pronounced conductance peak located at $\sim 7.7 \times 10^{-3} G_0$ (the lower panel of Fig. 14), which is in agreement with previously reported results on the single BPDT molecule conductance [23]. Since the BPDT molecule has a longer molecular distance than the solvent molecule and the thiol end group at both ends which chemically bonds strongly to apex gold atoms, we can expect that the most of the conductance values will originate from the BPDT molecule even though there may be some of the solvent molecules phyisiorbed on the surface of the gold tips. Notably, we are also able to observe variation of the conductance in each conductance plateau as the junction is pulled (black arrows in the upper panel of Fig. 14), which is possibly due to the mechanical response from the molecule-electrode coupling [24].

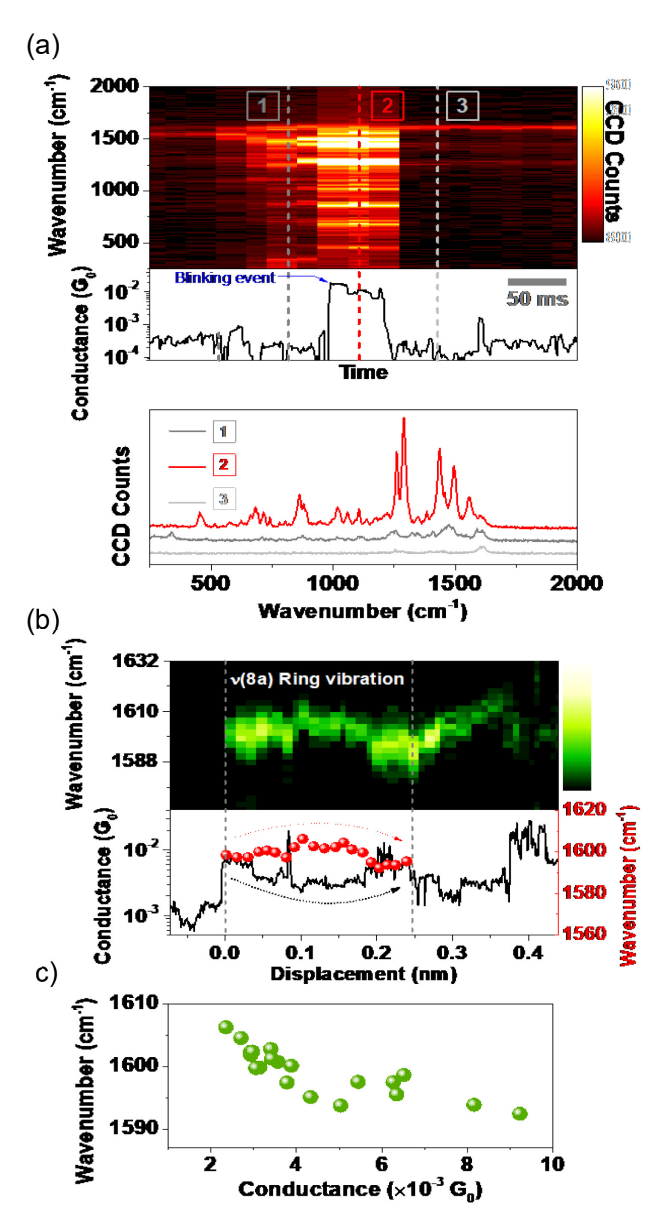


Fig. 15. Correlated pulling Raman and conductance measurement. (a) Real-time measurement of correlated Raman spectra and molecular conductance of the BPDT molecule. Raman spectra at three different times denoted as 1, 2, and 3 are depicted in the bottom plot. Each spectra is offset vertically for clarity. (b) Top panel: Zoomed-in intensity map of $\nu(8a)$ ring vibration mode over time. Bottom panel: Associated conductance trace over times (black curve) and extracted $\nu(8a)$ mode peak position from the top panel (red circles). (c) Combined conductance and Raman measurement plot from 0 to \sim 0.25 nm in the bottom panel of (b).

D. Pulling Measurement of Correlated Raman and Conductance

One distinctive strength of our MEMS-BJ system is the straightforward accessibility for optical characterization of a single-molecule junction due to its fully lateral architecture. Also, the demonstrated nanometer-scale controllability of the gap width coupled with inherent vibration-insensitivity to the external vibrational sources allows our system to act as a reliable testbed for the multi-dimensional (i.e. electrical, mechanical, and optical) characterization of a single-molecule junction. For this purpose, mechanically controllable break

junction system also can be utilized due to the similar fully lateral architecture. But still our system has potential advantages such as the stable focal distance, scalable production, and unnecessity of external apparatus (e.g. a piezo motor) [25]. In order to demonstrate such an advantage, first we perform Raman spectroscopy measurements on a BPDT singlemolecule junction by measuring the real-time Raman spectra correlated with molecular conductance traces as shown in Fig. 15(a). Here, we use a 785 nm laser light source (~ 3 mW laser intensity) with a 100× objective lens to collect Raman spectral data with 22 ms integration time while the electrical conductance data of the junction is being recorded simultaneously at 50 mV bias. Especially here, we have been trying to maintain the best consistency of the measurements by regulating the laser intensity, setting the best focus to collect the maximum signal, and probing the same hotspot (i.e. the nanogap between the gold electrode tips) as much as possible. However, note that more detailed analysis on the efficiency of the Raman measurements is necessary for a rigorous quantification of our multi-dimensional measurements. Details about the procedure of the Raman measurements are reported in our previous work [25]. Due to the junction-enhanced Raman scattering (JERS) effect [26], the Raman spectra is amplified and perturbed from normal Raman scattering (e.g. new peaks appear, the peaks are shifted from the supposed Raman shift of BPDT molecule) when a typical blinking event occurs. These fluctuations in the Raman spectra indicate dynamic processes in the single-molecule junction that occur due to the intrinsic stochastic nature of the single-molecule junction system. For example, the change in the molecular configuration on the metal surface could be attributed to these fluctuations [27]. Therefore, obtaining the simultaneous information of a singlemolecule on multi-dimensional aspects will allow us to gain insights on the dynamics of a single-molecule junction.

To demonstrate an example study of such a multi-dimensional approach by correlating electrical, optical and mechanical information, we focus on mechanical strain-induced modulation of electrical and optical characteristics of the BPDT single-molecule junction. Fig. 15(b) (c) show correlated Raman and conductance results of a BPDT single-molecule junction under mechanical strain. When a single-molecule junction is detected (the bottom panel of Fig. 15(b)) by the automated algorithm we described in Fig. 11, the controller applies decreasing actuation voltage to the comb electrodes which slowly pulls away the movable electrode from the fixed electrode to exert mechanical strain. Until the detection, the actuation voltage remained steady where the junction is in the tunneling regime to stochastically trap a single-molecule. From the measurement, we observe two important aspects: first in some cases, a 'bowl'-shaped conductance evolution is observed when the single-molecule junction is strained (black curve from 0 to ~0.25 nm in the bottom panel of Fig. 15(b), gray dashed lines guide for the eyes). This 'bowl'-shaped conductance behavior has been demonstrated to occur as a characteristic of strain-induced resonance in benzene-4,4'-dithiol (BDT) molecular junctions [28, 29]. When the junction is compressed, the BDT molecule is almost lying down between the electrodes, which causes an increase in conductance due to lateral π electron coupling between the molecule and electrodes [30, 31]. When the junction is stretched, however, electronic coupling

between the molecule and electrodes is reduced while the tunneling barrier width increases resulting in decrease in conductance. On the other hand, if the junction is stretched even further, the electronic coupling becomes weaker causing a shift in the highest occupied molecular orbital level of the molecule towards the Fermi energy of the electrodes, resulting in a corresponding increase in the conductance [24]. The BPDT molecule could exhibit similar behavior as the BDT molecule due to the similarities in their aromatic structure. From this analysis, we can expect that the blinking event in Fig. 15(b) occurred from a single-molecule junction formed in a compressed configuration in comparison to its equilibrium geometry. Second, corresponding to the strain-induced conductance evolution, we observe the v(8a) characteristic ring vibration mode shifts throughout the measurement. The red circles in the bottom panel of Fig. 15(b) shows the extracted peak position of the mode from the top panel of Fig. 15(b). As shown in the plot, the extracted peak position shows an antisymmetric correlation to the conductance evolution. This antisymmetric correlation is more clearly observable from the combined conductance and Raman measurement plot in Fig. 15(c). Theoretical studies anticipate that the vibrational mode will downshift to the lower energy upon stretching of a molecule due to increase of bond anharmonicity [32, 33]. This result supports the presumption that the 'bowl'-shaped conductance evolution in Fig. 15(b) originates from straininduced compression followed by stretching of the singlemolecule junction. Thus, by correlating the extracted multidimensional information from a molecular junction, we can pursue a deeper study of these dynamic features of the singlemolecule junction.

VII. CONCLUSION

In summary, we propose a robust lab-on-a-chip system for multi-dimensional (electrical, optical, and mechanical) characterization of a single-molecule utilizing a Si micromachined MEMS chip on an SOI wafer. The chip is delicately designed in order to ensure a sufficient actuation force with sub-nanometer displacement resolution and controllability using an electrostatic comb actuation scheme. Basic performance parameters of the designed chip such as an actuation displacement and pull-in voltage are analyzed using FEA-based simulations. In addition, the actuated displacement is successfully confirmed by measuring the corresponding capacitance change of the capacitive sensor array due to the displacement. Given the performance, we extend our study to use the chip for the multi-dimensional characterizations of a single-molecule junction. Specifically, we develop an automated algorithm to detect and pull a single-molecule junction while recording the Raman spectra simultaneously. The performance of the algorithm and measurement system is verified with a bare gold-gold contact by analyzing the decaying property of a tunneling current through the air. In addition, we were able to statistically investigate the electrical characteristics of a BPDT molecule at the single-molecule level using the break junction system. Finally, we demonstrate an example study of such a multi-dimensional approach by correlating electrical, optical, and mechanical information: mechanical strain-induced modulation of electrical and optical

characteristics of the BPDT single-molecule junction. From the experiment, it is found that the 'bowl'-shaped conductance evolution in the junction can be attributed to strain-induced compression or stretching of the single-molecule junction. Based on our results, we believe that our MEMS-BJ system will provide new insights on opto-electromechanical characteristics of a single-molecule promoting the development of new modalities for chemical and biological applications.

REFERENCES

- D. G. de Oteyza et al., "Direct imaging of covalent bond structure in single-molecule chemical reactions," Science, vol. 340, no. 6139, pp. 1434-1437, Jun. 2013.
- [2] Y. Li et al., "Detection and identification of genetic material via single-molecule conductance," Nat. Nanotechnol., vol. 13, no. 12, pp. 1167-1173, Dec. 2018.
- [3] S. H. Qian, S. Sun, Y. H. Wang, Z. J. Li, and H. W. Lin, "Recent advances of multidimensional sensing: from design to applications," *Sci. China Chem.*, vol. 62, no. 12, pp. 1601-1618, Dec. 2019.
- [4] G. H. Bardy *et al.*, "Amiodarone or an implantable cardioverter-defibrillator for congestive heart failure," *N. Engl. J. Med.*, vol. 352, no. 3, pp. 225-237, Jan. 2005.
- [5] V. Kutyifa et al., "Multicenter automatic defibrillator implantation trialsubcutaneous implantable cardioverter defibrillator (MADIT S-ICD): Design and clinical protocol," Am. Heart J., vol. 189, pp. 158-166, Jul. 2017.
- [6] V. C. Shukla et al., "Lab-on-a-chip platforms for biophysical studies of cancer with single-cell resolution," *Trends Biotechnol.*, vol. 36, no. 5, pp. 549-561, May. 2018.
- [7] T. Hirano, D. Kobayashi, T. Furuhata, and H. Fujita, "Electroplated and dry-released metallic microstructures for a lateral tunneling unit application," *Jpn. J. Appl. Phys.*, vol. 33, no. 2, pp. 1202-1208, Feb. 1994.
- [8] T. Tsuchiya, T. Hemmi, J. Y. Suzuki, Y. Hirai, and O. Tabata, "Tensile strength of silicon nanowires batch-fabricated into electrostatic MEMS testing device," *Appl. Sci.*, vol. 8, no. 6, Jun. 2018, Art. no. 880.
- [9] J. M. van Ruitenbeek et al., "Adjustable nanofabricated atomic size contacts," Rev. Sci. Instrum., vol. 67, no. 1, pp. 108-111, Jan. 1996.
- [10] K. Gall, J. K. Diao, and M. L. Dunn, "The strength of gold nanowires," *Nano Lett.*, vol. 4, no. 12, pp. 2431-2436, Dec. 2004.
- [11] H. D. Espinosa and B. C. Prorok, "Size effects on the mechanical behavior of gold thin films," *J. Mater. Sci.*, vol. 38, no. 20, pp. 4125-4128, Oct. 2003.
- [12] M. Bao, "Analysis and design principles of MEMS devices," Amsterdam, Netherlands: Elsevier, 2005, pp. 213-245.
- [13] Y. Sun, S. N. Fry, D. P. Potasek, D. J. Bell, and B. J. Nelson, "Characterizing fruit fly flight behavior using a microforce sensor with a new comb-drive configuration," *J. Microelectromech. Syst.*, vol. 14, no. 1, pp. 4-11, Feb. 2005.
- [14] N. Lafitte et al., "Improvement of silicon nanotweezers sensitivity for mechanical characterization of biomolecules using closed-loop control," *IEEE/ASME Trans. Mechatronics*, vol. 20, no. 3, pp. 1418-1427, Jun. 2015.
- [15] H. D. Espinosa, Y. Zhu, and N. Moldovan, "Design and operation of a MEMS-based material testing system for nanomechanical characterization," *J. Microelectromech. Syst.*, vol. 16, no. 5, pp. 1219-1231, Oct. 2007.
- [16] M. Labbane, N. K. Saha, and E. C. Ting, "Yield criterion and loading function for concrete plasticity," *Int. J. Solids Struct.*, vol. 30, no. 9, pp. 1269-1288, 1993.
- [17] S. W. Yoon, "Vibration isolation and shock protection for MEMS," Ph.D. dissertation, Dept. Elect. Eng., Univ. Mich., Ann Arbor, MI, USA, 2009.
- [18] Pull-In Voltage for a Biased Resonator—3D, COMSOL Inc., Burlington, MA, USA
- [19] B. Q. Wu, A. Kumar, and S. Pamarthy, "High aspect ratio silicon etch: A review," J. Appl. Phys., vol. 108, no. 5, Sep. 2010, Art. no. 051101.
- [20] H. H. Yang, C. K. Chao, M. K. Wei, and C. P. Lin, "High fill-factor microlens array mold insert fabrication using a thermal reflow process," *J. Micromech. Microeng.*, vol. 14, no. 8, pp. 1197-1204, Aug. 2004, Art. no. PII:S0960-1317(04)76199-9.
- [21] G. Binning, H. Rohrer, C. Gerber, and E. Weibel, "Surface studies by scanning tunneling microscopy," *Phys. Rev. Lett.*, vol. 49, no. 1, pp. 57-61, 1982.

- [22] T. Wang, W. Du, N. Tomczak, L. J. Wang, and C. A. Nijhuis, "In operando characterization and control over intermittent light emission from molecular tunnel junctions via molecular backbone rigidity," *Adv. Sci.*, vol. 6, no. 20, Oct. 2019, Art. no. 1900390.
- [23] R. Ramachandran, H. P. B. Li, W. Y. Lo, A. Neshchadin, L. P. Yu, and J. Hihath, "An electromechanical approach to understanding binding configurations in single-molecule devices," *Nano Lett.*, vol. 18, no. 10, pp. 6638-6644, Oct. 2018.
- [24] C. Bruot, J. Hihath, and N. J. Tao, "Mechanically controlled molecular orbital alignment in single molecule junctions," *Nat. Nanotechnol.*, vol. 7, no. 1, pp. 35-40, Jan. 2012.
- [25] H. Jeong, H. B. Li, L. Domulevicz, and J. Hihath, "An on-chip break junction system for combined single-molecule conductance and Raman spectroscopies," *Adv. Funct. Mater.*, vol. 30, no. 28, Jul. 2020, Art. no. 2000615.
- [26] F. Benz et al., "Single-molecule optomechanics in "picocavities"," Science, vol. 354, no. 6313, pp. 726-729, Nov. 2016.
- [27] D. R. Ward et al., "Simultaneous measurements of electronic conduction and Raman response in molecular junctions," *Nano Lett.*, vol. 8, no. 3, pp. 919-924, Mar. 2008.
- [28] R. B. Pontes, A. R. Rocha, S. Sanvito, A. Fazzio, and A. J. R. da Silva, "Ab initio calculations of structural evolution and conductance of benzene-1,4-dithiol on gold leads," ACS Nano, vol. 5, no. 2, pp. 795-804, Feb. 2011
- [29] N. Sergueev, L. Tsetseris, K. Varga, and S. Pantelides, "Configuration and conductance evolution of benzene-dithiol molecular junctions under elongation," *Phys. Rev. B*, vol. 82, no. 7, Aug. 2010, Art. no. 073106.
- [30] I. Diez-Perez et al., "Controlling single-molecule conductance through lateral coupling of pi orbitals," Nat. Nanotechnol., vol. 6, no. 4, pp. 226-231, Apr. 2011.
- [31] J. S. Meisner, M. Kamenetska, M. Krikorian, M. L. Steigerwald, L. Venkataraman, and C. Nuckolls, "A single-molecule potentiometer," *Nano Lett.*, vol. 11, no. 4, pp. 1575-1579, Apr. 2011.
- [32] V. K. Mitra, W. M. Risen, and R. H. Baughman, "Laser Raman study of stress dependence of vibrational frequencies of a monocrystalline polydiacetylene," *J. Chem. Phys.*, vol. 66, no. 6, pp. 2731-2736, 1977.
- [33] R. P. Wool, "Mechanisms of frequency shifting in infrared-spectrum of stressed polymer," *J. Polym. Sci. Pol. Phys.*, vol. 13, no. 9, pp. 1795-1808, 1975.



Hyunhak Jeong received the B.S. and Ph.D. degree in physics from Seoul National University, Seoul, South Korea, in 2009 and 2018, respectively. From 2018, he is currently a postdoctoral researcher with the Department of Electrical and Computer Engineering, University of California, Davis.

During his postdoctoral research, he has developed a robust single-molecule junction platform using a microelectromechanical system for optical, electrical characterizations of the single-molecule junction. His research interest includes understating of the physical properties of a single-molecule junction, fabrication of nanoscale electronic devices using nanomaterials, and development of novel microelectromechanical system chips for sensing applications.



Lucas K. Domulevicz received his B.S degree in electrical engineering and B.A. degree in Physics with minor focuses in mathematics and computer engineering from Wilkes University, Wilkes-Barre, Pennsylvania, in 2016. He is currently pursuing a Ph.D. degree in electrical engineering from the University of California, Davis.

From 2012 to 2016, he worked as a student research assistant at Wilkes University with a focus on computational chemistry and computational solid-state physics. In the summer of 2014, he participated in research at the University of Arkansas, Fayetteville, characterizing band structures of group IV alloys for use in optoelectronic devices as part of the national science foundation (NSF) research experience for undergraduates (REU) program. His current research focuses on using single-molecule Raman spectroscopy and computational simulations to understand how the structure of a molecule affects its ability to transport and convert different forms of energy for applications in molecular-scale electronics.

He is a recipient of the 2018 Science, Mathematics, and Research for Transformation (SMART) scholarship awarded by the United States Department of Defense and sponsored by the Naval Information Warfare Center Pacific (NIWC).



Joshua Hihath (SM'18) received a B.S. in Electrical Engineering from Kettering University in Flint, Michigan, and M.S. and Ph.D. degrees in Electrical Engineering from Arizona State University in Tempe, Arizona.

He previously worked as an Assistant Research Professor in the Center for Bioelectronics and Biosensors at the

Biodesign Institute at Arizona State University. Currently, he is an Associate Professor and Vice Chair for Undergraduate Studies in the Department of Electrical and Computer Engineering at University of California, Davis. His work is centered at the nexus of engineering, physics, chemistry and biology. This work focuses on understanding the electrical and mechanical properties of nanoscale and molecular systems, and has three primary thrusts: developing a fundamental understanding of charge transport and energy conversion at the single-molecule level; developing functional electronic devices from single-molecule and hybrid 2-dimensional systems; and utilizing single-molecule transport properties for biomedical applications.